Soft Matter

ARTICLE TYPE

Cite this: DOI: 00.0000/xxxxxxxxxx

# Dynamic and mechanical evolution of an oil-water interface during bacterial biofilm formation†

David P. Rivas,[a] Nathan D. Hedgecock,[a], Kathleen J. Stebe[b], and Robert L. Leheny[a]

Received Date
Accepted Date

DOI: 00.0000/xxxxxxxxxx

We present an experimental study combining particle tracking, active microrheology, and differential dynamic microscopy (DDM) to investigate the dynamics and rheology of an oil-water interface during biofilm formation by the bacteria *Pseudomonas Aeruginosa* PA14. The interface transitions from an active fluid dominated by the swimming motion of adsorbed bacteria at early age to an active viscoelastic system at late ages when the biofilm is established. The microrheology measurements using microscale magnetic rods indicate that the biofilm behaves as a viscoelastic solid at late age. The bacteria motility at the interface during the biofilm formation, which is characterized in the DDM measurements, evolves from diffusive motion at early age to constrained, quasi-localized motion at later age. Similarly, the mobility of passively moving colloidal spheres at the interface decreases significantly with increasing interface age and shows a dependence on sphere size after biofilm formation that is orders-of-magnitude larger than that expected in a homogeneous system in equilibrium. We attribute this anomalous size dependence to either length-scale-dependent rheology of the biofilm or widely differing effects of the bacteria activity on the motion of spheres of different sizes.

## 1 Introduction

Biofilms, assemblies of microbes in a self-produced conglomeration of extracellular polymeric substances (EPS), play a crucial role in the growth, protection, and dispersal of many bacteria species. Biofilms are abundant in nature and adept at existing in even extremely harsh environments. It has been estimated that 99% of all bacteria cells reside within biofilms, making them of fundamental importance to the life cycle of nearly all bacterial species. Some of the survival advantages associated with biofilm formation include protection from shear stress, desiccation, radiation, antibiotic and chemical threats, osmotic stress, and attacks from host immune cells, as well as more efficacious gene transfer[1]. The robustness of biofilm communities and their ability to survive in a wide range of environments also make them difficult to eliminate in undesirable settings. Biofilms are responsible for recurrent infections, contamination of medical and food processing equipment[2], and fouling of underwater equipment and ship surfaces[3]. Biofilms have also been utilized in constructive ways in environmental and industrial applications. For example, biofilms formed by hydrocarbon-consuming bacteria have been used in bioremediation of marine oil spills where they form at oil-water interfaces[3]. They have also been used for electrical energy extraction in microbial fuel cells[4,5]. Therefore, understanding the material properties of these films is valuable in development of strategies for their removal, prevention, or optimization in these contexts.

In general, biofilms can form at liquid-solid, liquid-air (where they are known as pellicles), or liquid-liquid interfaces. Biofilm formation involves the attachment or adsorption of the bacteria onto a solid or fluid interface followed by the secretion of EPS components by the cells[6]. The EPS can encase the cells in an extracellular matrix that consists primarily of polysaccharides, proteins, and nucleic acids. The mechanical integrity of the matrix is mostly due to the polysaccharides and proteins that often form a crosslinked viscoelastic polymer gel[7]. The viscoelastic properties of the film allow it to resist deformation when subject to small stresses while also avoiding brittle fracture under large external stresses[8]. However, a biofilm's structure and mechanical properties can vary greatly depending on the particular organism creating it and its local environment[9]. In fact, bacteria have been shown to change the amount of polymers they secrete and the cohesive strength of biofilms according to changes in their environment[10,11]. Experiments have shown that biofilm properties and growth rate at liquid-liquid and liquid-air interfaces are influenced by many factors, including the hydrophobicity of the bacteria, the surface tension of the interface, the subphase pH,

---

[a] *Department of Physics and Astronomy, Johns Hopkins University, Baltimore, MD, USA, 21218*

[b] *Department of Chemical and Biomolecular Engineering, University of Pennsylvania, Philadelphia, PA, USA, 19104*

† Electronic Supplementary Information (ESI) available: [details of any supplementary information available should be included here]. See DOI: 10.1039/cXsm00000x/

and the bacteria growth medium[12–14]. Biofilms are also naturally heterogeneous[15] and hence can potentially display length-scale dependent rheology. Consequently, conventional macrorheological studies effectively provide an average of the film's mechanical properties[6,13,16,17]. Microrheology is able to probe the heterogeneity of a film, but relating the mobility of colloidal probes, especially in passive microrheology measurements, to the interfacial rheology can be difficult[18,19].

Although much work has focused on the mechanical properties of biofilms that form on solid surfaces, relatively few studies have addressed films at liquid-air or liquid-liquid interfaces[6,12–15,17,20–24]. Fewer still have characterized the time evolution of biofilm rheology during the formation process, which is of interest from both a biological and physical perspective. In addition to the practical importance of biofilm properties at water-oil interfaces, which are particularly relevant in applications such as bioremediation and oil recovery, liquid-liquid interfaces provide unique environments in which hydrodynamics, physiochemical effects, and interfacial tension can conspire for intriguing outcomes[14,25–27].

In this paper, we report a study combining passive particle tracking, active microrheology, and differential dynamic microscopy (DDM) to gain a comprehensive perspective on the evolution in mechanics and dynamics of an oil interface with a bacteria suspension during biofilm formation. We use the bacteria strain *Pseudomonas Aeruginosa* PA14 (wild type), a widely investigated model organism. Previous experiments using *Pseudomonas* have shown that a number of strains of the bacteria, including PA14, form viscoelastic biofilms over the course of several hours at an oil-water interface[14,24]. Vaccari and coworkers employed particle tracking with 1-$\mu$m-diameter colloidal spheres in concert with pendant drop elastometry to characterize the interfacial dynamics and mechanics of suspensions of *Pseudomonas* sp. in contact with hexadecane[24]. They found that the evolution in the interface could be divided into three stages: an initial active stage in which the dynamics are dominated by the motile bacteria collecting at the interface, a transitional viscoelastic phase in which mean-square displacements of colloidal probes at the interface follow weak power laws, and a final elastic stage in which the interface acquires a bending rigidity. The work by Niepa *et al.* studied two strains of *Pseudomonas Aeruginosa*, PA14 and PA01, as well as mutants of these strains in which certain genes associated with secretion of EPS components or with the growth of pili were deleted[14]. They found that 1-$\mu$m-diameter passive tracers transitioned from super-diffusive to subdiffusive motion on the order of hours consistent with the stages of biofilm development identified by Vaccari *et al.*, although the films showed different properties depending on the bacterial strain, particularly at late ages. For example, PA01 strains became elastic after several hours, as determined by cessation of colloidal motion and the observation of wrinkles during compression of pendent drops, while PA14 strains did not. The mutant strains had a lower degree of film elasticity or formed a biofilm at later ages compared to the wild-type strains, thus demonstrating correlations between the bacteria's genetic makeup and the resulting biofilm properties.

Although such previous studies have shown how the passive tracking of colloidal probes can sensitively detect changes in an interface during biofilm formation, significant open questions remain. One important question is how to interpret probe mobility in terms of material properties in these heterogeneous and active films, where the application of generalized Stokes-Einstein relations used in microrheology of equilibrium systems[28,29] is not necessarily valid. Indeed, the dynamics of passive colloidal probes interacting with motile bacteria have been the subject of extensive work, where the probe motion has provided a window into the nature of the bacteria suspensions as an example of "active matter"[30–37]. In this regard, interfacial biofilms provide an intriguing experimental system for studying active systems within viscoelastic environments[38]. To help gain insight into this issue, we conducted experiments in which we tracked passively moving spherical colloids at an interface during film formation in parallel with active microrheology measurements involving the rotation of microscale magnetic rods at the interface in response to time-varying magnetic fields. We studied the colloidal dynamics during a transition from an active-fluid environment prior to biofilm formation into an active viscoelastic state during and after biofilm formation. The mechanical properties of the interface that one would infer from the passive and active measurements are strongly different. We attribute the discrepancy to the differing length scales over which the film properties are interrogated by the spheres versus the rods and to the differing effects of the activity of the motile bacteria in each case. To gain an understanding of the influence of each of these factors, we employed colloidal probes of varying sizes in the passive measurements and conducted differential dynamic microscopy (DDM) measurements in parallel to elucidate the evolution in bacteria motion during film formation.

## 2 Materials and Methods

### 2.1 Magnetic Microrods and Fluorescent Spherical Colloids

The microscale magnetic rods used to probe the micromechanics of the interface were composed of ferromagnetic nickel and were fabricated by electrodeposition following procedures described elsewhere[39]. The rods, 370 nm in diameter and 30-75 $\mu$m in length, possessed a magnetic moment parallel to their axis that was proportional to their length and was approximately $1.5 \times 10^{-12}$ A/m$^2$ for a 50-$\mu$m-long rod. The passive particle-tracking experiments employed fluorescent, non-functionalized, polystyrene spheres (Bangs Laboratories) of three diameters: 1 $\mu$m, 4 $\mu$m, and 15 $\mu$m. These diameters span scales from less than the bacteria cell size (1-5 $\mu$m length[40,41]) to up to several times larger than this, providing a useful range for probing the local rheology at the relevant length scales. The 1-$\mu$m diameter spheres (Bangs, cat. no. FSDG005) and 15-$\mu$m diameter spheres (Bangs, cat. no. FSDG009) were internally dyed with "Dragon Green" fluorescent fluorophores (480 nm excitation, 520 nm emission), while the 4-$\mu$m-diameter spheres (Bangs, cat. no. FSFR006) contained "Flash Red" fluorophore (660 nm excitation, 690 nm emission).

### 2.2 Bacteria Suspension Preparation

We used *Pseudomonas Aeruginosa* PA14 (wild-type) strain for all experiments involving interfacial film formation. Additional particle tracking and microrheology with the rods at the interface in the absence of a film were performed using *Pseudomonas Aeruginosa* PA14 ΔPelA, a mutant that has the pelA gene deleted thereby rendering the bacteria unable to form the extracellular matrix[14]. The bacteria were grown in LB broth medium while shaken at 200 RPM for approximately 36-48 hours at room temperature until the stationary phase of growth was reached. A portion of the broth was extracted and centrifuged at 6000 g for 10 minutes. The supernatant was discarded, and the bacteria were resuspended in 0.85% NaCl solution. This was repeated four times. The final cell concentration of the suspensions used in the experiments was $(1.65 \pm 0.05) \times 10^{10}$ cells per mL, as measured with a hemocytometer. Since the bacteria were without nutrient during the experiments, this concentration was assumed to remain fixed, and indeed no evidence of cell growth during the measurements was observed.

### 2.3 Sample Preparation

The sample cells were composed of aluminum rings, 1-cm inner in diameter and 0.8 cm in height. Glass slides attached to the rings with an optical adhesive (Norland Products) served as the sample-cell bottoms for viewing from below. The rings were cleaned by scrubbing with a detergent then sonicating in acetone followed by isopropyl alcohol and deionized water. The substrate and ring were then hydrophobically treated with Aquapel (Pittsburgh Glass Works) or Rain-X water repellant, which aided in stabilizing a flat oil-water interface. Approximately 200 $\mu$L of HFE 7500 fluorinated oil (Ran Biotechnologies) was pipetted into the ring. The viscosity of the oil is approximately equal to that of water, 1 mPa·s. The oil is denser than water, thereby allowing for viewing of the interface through the oil phase using an inverted microscope (see Fig. 1 for a schematic of the experiment). Bacteria suspension containing fluorescent spheres and ferromagnetic rods was then pipetted onto the surface of the oil to form the interface, and the top of the sample cell was covered with a coverslip to prevent evaporation. Since the spheres and rods are denser than water, they sedimented and became attached to the interface over the course of several minutes. The age of the interfaces $t_a$ was taken as the time since the bacteria suspension was added atop the oil.

### 2.4 Video Microscopy

Bright-field and fluorescence microscopy measurements were performed using an inverted optical microscope (Nikon Eclipse TE2000). Magnetic fields were applied by an array of four pairs of magnetic solenoids mounted to the microscope and controlled with custom Labview code, as described elsewhere[42]. Fluorescent microscopy was conducted using an X-Cite 120PC mercury arc lamp light source. CY5 (Nikon) and FITC (Omega Optical) filter cubes were used for fluorescent imaging of spheres labeled with “Flash Red” and “Dragon Green” fluorophores, respectively.

Videos were acquired using a 20X objective (Nikon, CFI 40 LWD DL) and a Flare CameraLink camera (IO Industries) connected to the microscope. Typically, 1000 frames were captured at 3 frames per second (fps) for passive particle-tracking experiments of the spherical colloids. Additional measurements at frame rates of 0.4 and 30 fps were also conducted to extend the dynamic range. A frame rate of 30 fps was employed for all measurements of the rod response to external magnetic fields, and frame rates between 20 and 30 fps were used for passive particle-tracking measurements on the rods.

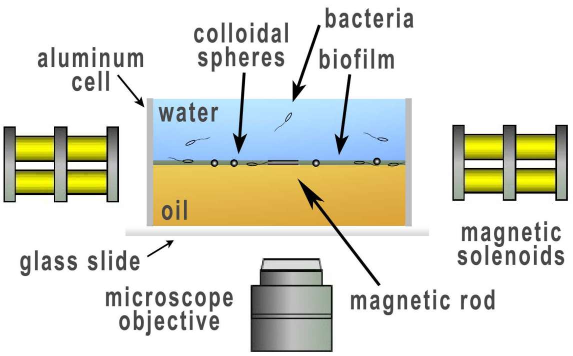

Fig. 1 Schematic of the experimental system. An aqueous suspension of bacteria containing micrometer-scale, fluorescently labeled spheres and ferromagnetic rods is pipetted over a layer of oil. The spheres and rods sediment to the interface and bacteria adsorb to the interface where they form a biofilm. The spheres and rods are used in passive particle tracking and active microrheology experiments. The interface is imaged using an inverted fluorescence microscope equipped with a set of four pairs of solenoids (two shown) for applying *in situ* magnetic fields.

### 2.5 Passive Particle Tracking

Passive particle-tracking measurements were performed using both the spherical colloids and the magnetic rods. The positions of the fluorescent spherical particles were tracked and their trajectories determined using custom Python code[43] based on the Crocker-Grier algorithm[44]. In a typical measurement, 100 to 500 particles were in the field of view. Overall drift of the particles was determined by finding the average motion of the colloids between adjacent frames and was subtracted from the individual trajectories. Despite this correction, we found that a small amount of residual drift affected the results in measurements where the colloid mobility was very small. We believe this residual drift was due to spatial variation in the drift velocity of the biofilm across the field of view. Segmentation of the frames into sections for more local drift determination was performed in instances where the residual drift was significant, thus producing sufficient improvement on some cases.

To characterize the statistical properties of the trajetories, we determined the time-average mean squared displacement (MSD) of each sphere,

$$\langle \Delta r_i^2(t) \rangle = \langle [\vec{r}_i(t+t') - \vec{r}_i(t')]^2 \rangle_{t'}, \tag{1}$$

where the subscript $i$ indicates the $i^{th}$ particle, and $t$ is the lag time, and the ensemble-averaged MSDs for each sphere size,

$\langle \Delta r^2(t) \rangle = \sum_i \langle \Delta r_i^2(t) \rangle$. The minimum resolvable ensemble MSD was estimated by measuring stationary 15-$\mu$m spheres attached to cover glass under identical microscope settings as in the experiments and was found to be approximately 0.001 $\mu$m$^2$.

To characterize the time-dependent position and orientation of the rods, we employed a custom Python code as described previously[45]. Briefly, the code first applied a thresholding of the images that zeroed all pixels below a certain intensity value. The rods were then located by determining the largest connected region of non-zero pixels. The position of the rod was taken as the center of mass of this region, and the orientation of the long axis of the rod was found by computing the eigenvectors of the moment of inertia tensor and identifying the direction of the rod axis with that of the eigenvector with the largest eigenvalue.

### 2.6 Magnetic Nanorod Active Microrheology

Two types of measurements involving the response of the rods to external fields were performed. In the early stage of the interface before biofilm formation, when the interfacial dynamics were dominated by motile bacteria, we applied fields of constant magnitude rotating in the plane of the interface, which caused the rods to rotate at constant angular velocity, and determined the effective interfacial viscosity from the rotational drag on the rods. Once the biofilm formed, the microrheology measurements were conducted by the application of step changes in the applied magnetic field. Starting initially from zero field, the applied field was ramped rapidly (rise time $< 2$ ms) to reach a constant field oriented in the plane of the film at an angle to a rod. The rod's orientation as a function of time was monitored as it rotated in response to the magnetic torque. As described below, the rod typically rotated until reaching an equilibrium orientation at which the magnetic torque was balanced with the elastic torque on the rod from the film. After some time, the field was then set back to zero, and the rod's orientation as a function of time was again monitored as it relaxed back toward its original orientation under the viscoelastic stresses of the film.

### 2.7 Differential Dynamic Microscopy

Differential dynamic microscopy (DDM)[46,47] measurements were performed to characterize the bacteria motion at the interface during film formation. Bright-field images were acquired and analyzed following the procedure described elsewhere[48]. Briefly, in a typical measurement 800 images were captured at 30 fps. The difference between all pairs of images in the sequence was determined, and the square of the Fourier transform of these differences as a function of wave vector $\vec{q}$ was calculated. Averages over wave-vector direction and over all pairs of frames separated by the same lag time $t$ were then taken to obtain the image structure function $D(q,t)$[46],

$$D(q,t) = \left\langle \left( \int \left( I(\vec{x},t'+t) - I(\vec{x},t') \right) e^{i\vec{q}\cdot\vec{x}} d^2\vec{x} \right)^2 \right\rangle \tag{2}$$

where $I(\vec{x},t')$ is the spatially-dependent intensity of the image acquired at time $t'$, and the brackets indicate averages over $t'$ and over wave-vector direction. Prior to calculation of $D(q,t)$, the image functions $I(\vec{x},t')$ were corrected for global drift by shifting the positions $\vec{x}$ in each frame relative to those of the preceding frame using Matlab's *imtranslate* function. Failure to account for drift in this way resulted in spurious oscillatory features in $D(q,t)$.

## 3 Results

Immediately following addition of the bacteria suspension atop the oil to form the oil-water interface, adsorbed bacteria were observed at the interface at high surface coverage. However, no collective swarming motion was observed. Hence, prior to film formation, the interface was densely populated by bacteria swimming randomly, creating an active fluid. At later interface ages, a viscoelastic film formed which gave the interface an overall darker and slightly mottled appearance and led to a large reduction in mobility of the tracer particles[24]. As mentioned above, in order to characterize the evolution of the dynamics and mechanical properties of the interface throughout the process of biofilm formation, we conducted particle-tracking experiments with colloidal probes of different sizes – specifically, spheres with diameters of 1 $\mu$m, 4 $\mu$m, and 15 $\mu$m – in parallel with particle tracking and microrheology measurements using ferromagnetic rods of length 30-75 $\mu$m and complementary DDM measurements to characterize the bacteria mobility at the interface. In the sections below, we describe the observations made with each experimental approach in turn and compare the results to interpret their implications for the mechanical and dynamical evolution of the interface.

### 3.1 Passive Particle Tracking

#### 3.1.1 Tracking of Spherical Colloids

Figure 2(a) displays the ensemble mean-squared displacement (MSD) of 4-$\mu$m spheres at various ages of an interface, while Fig. 2(b) shows ensemble MSDs for all three sphere sizes at interface ages $t_a = 1$ hr and 6 hrs. (For reference, bright-field microscopy videos of an interface containing the spheres at $t_a = 1$ hr and 7 hrs are included in the SI.) Also shown in Fig. 2(b) is the MSD measured on stationary 15-$\mu$m spheres as described in Sec. 2.5, which serves as a measure of the experimental resolution. For comparison, the MSD of the 4-$\mu$m spheres measured at the bare oil-water interface in the absence of bacteria is included in both figures. In the absence of bacteria, the spheres undergo simple diffusion with a diffusion coefficient consistent with the viscosity of the oil and water. The evolution in the particle mobility at the interface of the bacteria suspension follows qualitatively the trends reported previously by Vaccari *et al.*[24] At early ages the MSDs exceed those at the bare interface, indicating that the particle motion is enhanced by interactions with the motile bacteria. However, at later ages the particle mobility becomes increasingly suppressed, as shown by significant decreases in the MSDs, reflecting the formation and development of a viscoelastic interfacial film. Specifically, in Fig. 2(a) one sees a only a minor change in the MSDs between $t_a = 1$ hr and 3 hrs, but then a significant reduction in probe mobility between $t_a = 3$ hrs and 5 hrs. Results for the MSDs obtained during two additional experiments are included in the Supplementary Information (SI). In those cases, the

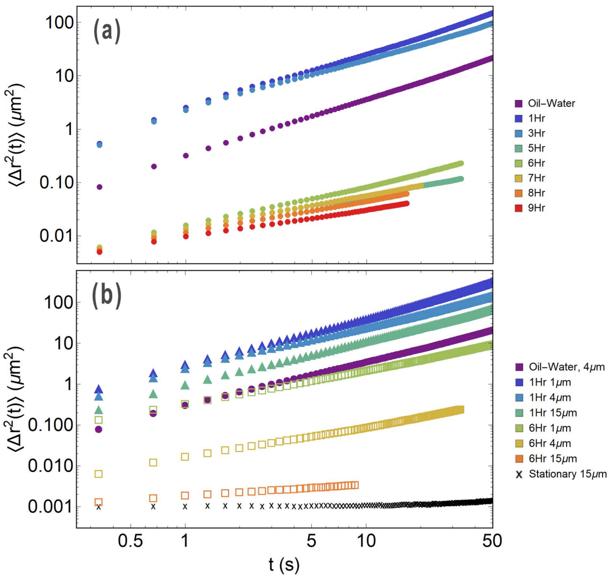

Fig. 2 (a) Ensemble mean-squared displacements of 4-$\mu$m-diameter spherical particles at the oil interface of the bacteria suspension at different interface ages, as indicated in the legend. (b) The mean-squared displacements of 1-$\mu$m, 4-$\mu$m, and 15-$\mu$m spheres at the interface at ages of 1 hr and 6 hrs, as indicated. Also shown in (b) is an estimate of the minimum resolvable ensemble MSD obtained from a measurement on stationary 15-$\mu$m spheres. Also shown in both panels is the mean-squared displacement of 4-$\mu$m-diameter spheres at the oil-water interface in the absence of bacteria. The frame rate in all measurements was 3 fps.

MSDs underwent a qualitatively similar reduction over the same time scale, but the changes were more continuous, indicating the variation in the evolution of probe dynamics that can occur under nominally identical experimental conditions.

A key feature of the particle mobility at the interface is the dependence on probe size and particularly the evolution in size dependence with interface age. As seen in Fig. 2(b), the mobilities of the different-sized probes diverge strongly from one another as the biofilm forms. At $t_a = 1$ hr, the MSDs of the 1-$\mu$m and 15-$\mu$m spheres have similar shape and differ by a modest factor of 3 to 4. This factor is even smaller than that predicted by the Stokes-Einstein relation, wherein the MSDs of colloids undergoing thermal Brownian motion are predicted to vary inversely with colloid diameter. This weak size dependence at the early interface age is consistent with models and previous experiments that show an enhancement in effective diffusivity of tracers in an active bath that is independent of tracer size[37,49]. It also potentially reflects effects similar to those reported by Patteson *et al.*, who observed diffusivities of probes in bacteria suspensions that varied non-monotonically with probe size[34]. The situation changes dramatically, however, at later ages when the influence of the biofilm is strong. For instance, after $t_a = 6$ hrs, the 15-$\mu$m spheres have become essentially static with an MSD, $\langle \Delta r^2(t) \rangle \approx 10^{-3}$ $\mu\text{m}^2$, that is close to the estimated measurement resolution, while the MSD of the 1-$\mu$m spheres exceeds this value by a factor of $10^2$ to $10^4$ over the range of lag times probed. The diverging probe mobilities are further illustrated in Fig. 3(a), which shows $\langle \Delta r^2(t) \rangle$ at $t = 10$ s as a function of age for the probes of different size. The very large difference in mobility with size at late age is particularly striking when considering that the interfacial stresses on the probes should become dominant with formation of the biofilm, and hence the hydrodynamics should become essentially two-dimensional. For a homogeneous film in equilibrium, the particle mobility would be independent of probe diameter to first order[50,51].

To characterize the evolution of the MSDs more quantitatively, we fit them to a power-law form, $\langle \Delta r^2(t) \rangle = bt^{\alpha}$, which in most cases provides a good approximation to the data at least over a limited range of lag times. To estimate the power-law exponents $\alpha$, we performed fits to each MSD over various ranges spanning one to two decades in lag time between 0.33 s and 33.3 s. The results are shown in Fig. 3(b), where error bars indicate the range of values obtained over different ranges of lag time. (In many cases the range was smaller than the symbols in the figure.) At the earliest age, $t_a = 1$ hr, the probes exhibit slightly super-diffusive motion ($\alpha > 1$), and then the motion becomes essentially diffusive ($\alpha \approx 1$) at somewhat later age, $t_a = 3$ hr. The reduction in mobility at $t_a = 5$ hr and above is accompanied by a transition to sub-diffusive motion ($\alpha < 1$), qualitatively consistent with previous results on 1-$\mu$m spheres at the interface of suspensions of PA14 and hexadecane[14,24]. Subdiffusive motion is often described by models such as caged-diffusion, continuous-time random walks, obstructed diffusion, or fractional Brownian motion[52]. We find that the spheres' velocity correlations within the biofilm are in good agreement with those predicted by a fractional Brownian motion model, which is often used to model particle motion in viscoelastic materials[53,54]. Details are provided in the SI. Notably, the divergence in the mobilities of the probes of different sizes is again apparent in this subdiffusive behavior of the MSDs, where, as seen in Fig. 3(b), $\alpha$ decreases more for the larger-diameter spheres.

For another perspective on the sphere motion in the biofilms, Fig. 4(a) displays the van Hove correlation function, which is the probability distribution of particle displacements, of the ensemble of 4-$\mu$m particles at a lag time of 0.33 s at $t_a = 9$ hrs. For particles in thermodynamic equilibrium, the van Hove function is Gaussian. In contrast, the spheres' van Hove function has large non-Gaussian tails reflecting excess probability of large displacements, as illustrated by the comparison with the Gaussian lineshape in Fig 4(a). While such non-Gaussian behavior can reflect a variety of out-of-equilibrium dynamical properties, in this case we can identify it with spatial heterogeneity of the dynamics. This heterogeneity is illustrated in Fig. 4(b), which displays examples of the van Hove correlation functions of two individual 4-$\mu$m spheres from the ensemble. Both individual correlation functions are Gaussian, which is what we find for the vast majority of the spheres at all ages. We show the MSDs of these two spheres in Fig. 4(c). Both particles display motion that is similarly sub-diffusive, but the curves are well separated throughout the experimental time frame, indicating a persistence to the heterogeneity in mobility over at least tens of seconds. Thus, the non-Gaussian character of the ensemble van Hove correlation function is a consequence of averaging over particles whose dynamics indi-

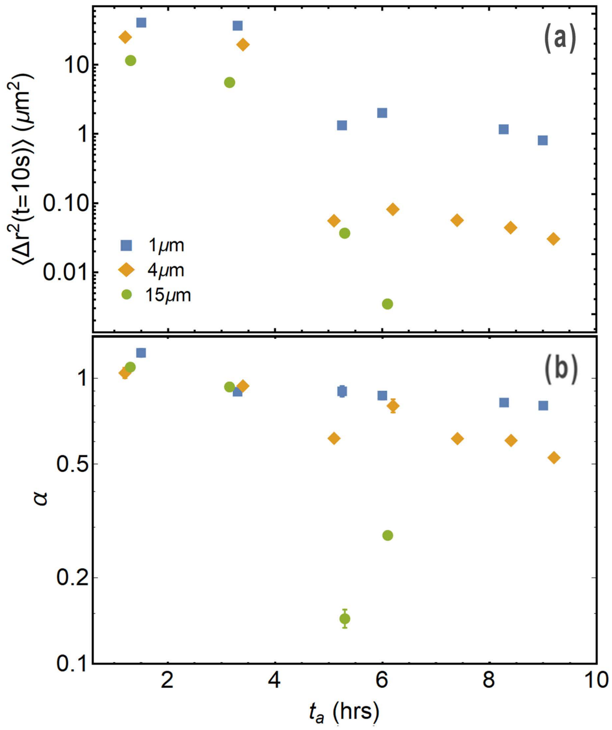

Fig. 3 (a) The mean-squared displacement of spheres of three diameters at a lag time of 10 s as a function of interface age. The mobility of the spheres, particularly that of the largest spheres, decreases significantly at an interface age of approximately 4 hours, which is associated with formation of the biofilm. (b) Power-law exponents obtained from fits to the mean-squared displacements of the spheres as a function of interface age. The sphere motion is slightly super-diffusive prior to biofilm formation and becomes subdiffusive once the biofilm forms.

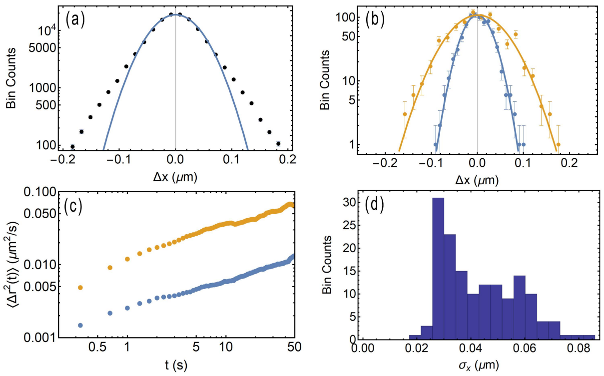

Fig. 4 (a) Ensemble-average van Hove correlation function of the displacement of 4-$\mu$m spheres over 0.33 s within a biofilm at an age of 9 hours. The solid blue curve shows a Gaussian fit to the data. (b) van Hove correlation functions for two individual spheres at the interface in comparison with Gaussian fits giving widths of $\sigma_x = 0.028$ $\mu$m and 0.055 $\mu$m. (c) The mean-squared displacements for the same two spheres. The consistency of their separation with lag time indicates a disparity in the mobility of the particles that persists at least tens of seconds. (d) The distribution of widths of the van Hove correlations of the ensemble, as determined by performing Gaussian fits to the van Hove correlation for each sphere.

vidually obey Gaussian statistics but with significant variation in mobility. Figure 4(d) shows the probability distribution of Gaussian widths $\sigma_x$ of the van Hove correlations of the individual 4-$\mu$m particles at $t_a = 9$ hrs, illustrating this large variation in mobility. The asymmetric shape of the distribution, with a tail to large $\sigma_x$, correlates with the excess probability in the van Hove function at large displacement.

Qualitatively similar results as those shown in Fig. 4 were found at all ages. Prior to biofilm formation, the large variances in $\sigma_x$ could be due to heterogeneities in the interface caused by spatial variations in the bacteria activity or by inhomogeneous distribution of EPS in the incipient film. Indeed, anecdotal observations of the interface at early age indicated that the colloids acted as nucleation sites of the viscoelastic biofilm, which could lead to a variation of effective particle sizes and hence diffusivity during incipient biofilm formation. We note that the particle trajectories had the character of random walks, and the more elaborate trajectories observed when colloids attach to swimming bacteria[55] were not observed.

### 3.1.2 Tracking of Rods

**3.1.2.1 Orientational Fluctuations** To gain another perspective on the mobility of colloidal tracers at the interface in the presence of the motile bacteria, we performed particle-tracking measurements of the passive motion of magnetic rods. To avoid the complication from biofilm formation in this case, we employed a mutant strain of *Pseudomonas Aeruginosa* with the pelA gene deleted, which rendered the bacteria unable to form the biofilm. Because of the rods' large magnetic moment $\mu$, the torques imposed by magnetic fields $B$ as small as earth's field constrain their orientation such that thermal orientational fluctuations are immeasurably small. For instance, in a 1 G field at room temperature, $\mu B/k_B T \sim 10^4$. However, consistent with the enhanced mobility of the spheres at early interface age, rods at the oil interface of the bacteria suspension underwent measurable orientational fluctuations. Figure 5(a) displays the angular MSD, $\langle\Delta\theta^2(t)\rangle = \langle[\theta(t') - \theta(t'+t)]^2\rangle_{t'}$, of a rod of length 29 $\mu$m at the active bacterial interface in the presence of a net field (applied field plus earth's field) of 1 G, where $\theta = 0$ is taken as the direction of the field. To interpret this correlation function, we assume an overdamped Langevin equation describing the rotational motion[56],

$$\gamma_R \eta_{eff} \dot{\theta} = \Gamma_B + \zeta_A(t) \tag{3}$$

where $\Gamma_B = \mu B \sin(\theta) \approx \mu B\theta$ is the magnetic torque, $\zeta_A(t)$ is a random active torque, $\eta_{eff}$ is the effective drag viscosity, $\gamma_R = \pi L^3/[3\,(ln(L/d) - 0.662 + 0.917L/d)]$ is the geometric drag coefficient of a rotating rod of length $L$ and diameter $d$[57], and we ignore random thermal forces since they are deemed insignificant in comparison to the active forces. (Note $\gamma_R$ is the coefficient for rod rotation in a bulk, three-dimensional fluid. As described below, $\gamma_R$ must be replaced with a two-dimensional version at later interface ages when the interfacial rheology of the biofilm dominates the rotational response.) Assuming correlations in the random active torques decay exponentially in time, $\langle\zeta_A(t'')\zeta_A(t')\rangle = \frac{D_A}{\tau}\exp(-|t''-t'|/\tau)$, we can use Eq. (3) to obtain an expression for $\langle\Delta\theta^2(t)\rangle$[56],

$$\langle\Delta\theta^2(t)\rangle = 2D_A\left[\frac{\tau_B(1-e^{-t/\tau_B}) - \tau(1-e^{-t/\tau})}{1-(\tau/\tau_B)^2}\right] + \Delta\theta_0^2 \tag{4}$$

where $\tau_B \equiv \gamma_R\eta_{eff}/\mu B$ sets the timescale at which the MSD becomes constrained by the magnetic torque, and $\Delta\theta_0^2$ is an offset introduced to account for digital noise.

A fit to $\langle\Delta\theta^2(t)\rangle$ using Eq. (4), shown by the line in Fig. 5(a), agrees well with the data and gives $\tau_B = 0.554 \pm 0.013$ s, $\tau = 0.082 \pm 0.007$ s, $D_A = (4.19 \pm 0.12) \times 10^{-3}$ s$^{-1}$, and $\Delta\theta_0^2 = (2.4 \pm 2.2) \times 10^{-5}$. The correlation time of the random active forces, $\tau$, is comparable to that obtained in particle tracking of colloidal spheres in other active bacteria suspensions[24,33,56]. Additionally, the value of $\tau_B$ provides a result for the rotational drag viscosity,

$$\eta_{eff} = \frac{\tau_B \mu B}{\gamma_R} \tag{5}$$

which is found to be $\eta_{eff} = (4.3 \pm 1.4) \times 10^{-3}$ Pa·s, where the primary source of error is the uncertainty in $B$. This value of the viscosity is 3-4 times that of the bulk oil and water subphases and is approximately twice that obtained in active microrheology measurements described below.

**3.1.2.2 Effective Temperature** The behavior of $\langle\Delta\theta^2(t)\rangle$ can be divided into three regimes. In the first, when $t \ll \tau$, the MSD increases ballistically, $\langle\Delta\theta^2(t)\rangle \approx 2D_At^2/[\tau(1-(\tau/\tau_B)^2]$. In the second, when $\tau_B \gg t \gg \tau$, the behavior is diffusive, $\langle\Delta\theta^2(t)\rangle \approx 2D_At$. Finally, at very large lag times, $t \gg \tau_B$, the MSD plateaus, $\langle\Delta\theta^2(t\to\infty)\rangle = 2D_A\tau_B/[1+\tau/\tau_B] \approx 2D_A\tau_B$. From this large-lag-time plateau, one can identify an "effective temperature" of the active bath,

$$T^R_{eff} = \frac{\mu B\langle\Delta\theta^2(t\to\infty)\rangle}{2k_B} \approx (32 \pm 10)T_{RT} \tag{6}$$

where $T_{RT} = 293$ K is room temperature. We note that in a typical passive microrheology measurement, one is only able to find an effective diffusivity and then must assume a value for the viscosity in order to extract an effective temperature. In contrast, measuring the motion of a probe within a potential energy well allows for the determination of both $\eta_{eff}$ and $T^R_{eff}$ from Eqs. (5) and (6), respectively.

Characterizing statistical averages of random motion in an active system in terms of an effective temperature is an established approach[58,59], although examples in which it breaks down are documented[37]. The notion of an effective temperature associated with the fluctuations in the rod's orientation is supported by the angular probability distribution function, which follows a Boltzmann-like form, as shown in the inset to Fig. 5(a). In general, such distributions in an active bath deviate from a Boltzmann-like form[25,37,60]. However, Boltzmann-like behavior seems to be recovered in confined systems like the magnetic rod in the external field. For instance, previous experiments on suspensions of active colloids under gravity found the height probability distribution exhibited a Boltzmann form with an effective temperature equal to that determined by their diffusive motion[59]. Additionally, experiments of an active system of particles in a harmonic potential found a Boltzmann probability distribution when the confinement size was much larger than the correlation length of the active swimmer's trajectories[61], and a similar result was found for a colloid trapped in a harmonic potential within a bacterial bath[62].

**3.1.2.3 Positional Fluctuations** In addition to measuring the rod's angular MSD, we tracked the center of mass of the rod to compare its translational and rotational mobilities. Analyzing the videos in the body frame of the rod, we separated the center-of-mass motion into components parallel and perpendicular to the rod axis. The resulting translational MSDs, shown in Fig. 5(b), vary approximately proportionally with lag time, implying effective diffusive motion, $\langle\Delta r^2_{\parallel,\perp}(t)\rangle = 2D_{\parallel,\perp}t$ over the range of lag times shown. From this diffusive motion, we can identify additional effective temperatures for each direction of motion,

$$T^{\parallel,\perp}_{eff} = \frac{\eta_{eff}\gamma_{\parallel,\perp}D_{\parallel,\perp}}{k_B} \tag{7}$$

where $\gamma_\parallel \approx 2\pi L/[ln(L/d) - 0.2]$ and $\gamma_\perp \approx 4\pi L/[ln(L/d) + 0.84]$ are the geometric drag coefficients of a rod translating parallel and perpendicular to its axis, respectively[63]. Based on the viscosity obtained from the rod's orientational fluctuations (Eq. (5)), we find $T^\parallel_{eff} \approx T^\perp_{eff} \approx (101 \pm 34)T_{RT}$. The approximate equality of $T^\parallel_{eff}$ and $T^\parallel_{eff}$ implies the ratio $D_\parallel/D_\perp$ is similar to that of thermal diffusion. Previous experiments by Peng *et al.* investigating the translational diffusion of ellipsoidal colloids in *E. Coli* suspensions within soap films[35,64] found that $D_\parallel/D_\perp$ was significantly smaller than expected from equilibrium at high bacterial concentrations. The authors of the study postulated that the persistence time of the anisotropic particle's motion along the minor axis was enhanced due to the effects of the extensile dipole flow field created by the swarming bacteria. Since we do not observe swarming in our system despite the high density of bacteria at the in-

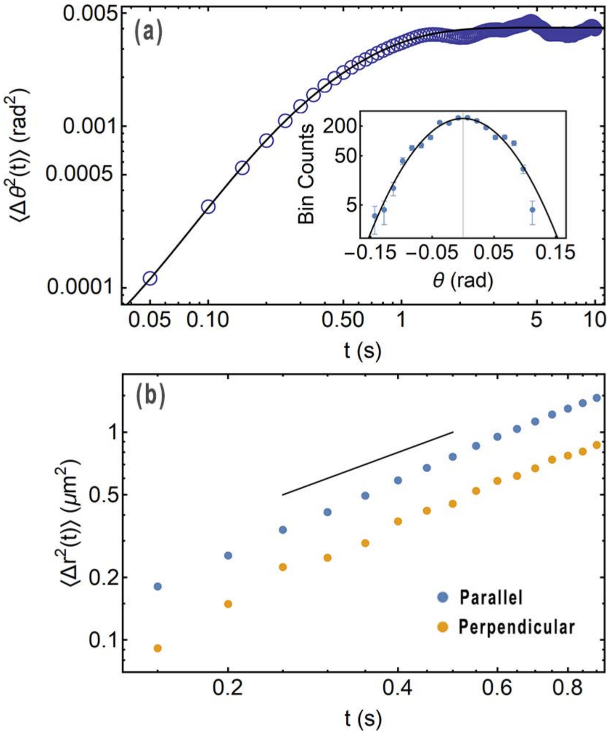

Fig. 5 (a) Rotational mean-squared displacement of a rod at the oil interface of a bacteria suspension in the absence of a biofilm and in the presence of a 1 G magnetic field in the plane of the interface. The solid curve shows a fit to the data using Eq. (4). Inset: The van Hove correlation function of the angle of the magnetic rod relative to its mean orientation, which corresponds to the direction of the magnetic field. The solid line shows a Gaussian fit to the data. The distribution is in good agreement with the Boltzmann form. (b) Mean-square displacements of the center of the rod in the directions parallel (blue) and perpendicular (orange) to the rod's axis. The solid line has a slope of one.

terface, the lack of anomalous diffusion between the parallel and perpendicular directions is consistent with this picture. However, we note that the effective temperature obtained from the translational diffusion is several times larger than that obtained from the rotational diffusion, which is also in contrast with the observations of Peng *et al.*[35,64] These contrasting trends between our results and those of Peng *et al.* indicate further study is needed to understand the mobility of anisotropic particles in active fluids. Beyond the lack of swarming in our experiments, another difference with the previous study that might play a role[65] is the particle aspect ratio, $p = L/R$. For the ellipoids investigated by Peng *et al.*, $p = 5.1$, but for the our rods, $p > 200$.

## 3.2 Active Microrheology

### 3.2.1 Rod Mobility at Early Interface Age

As a complementary method for investigating the evolution of the mechanics and dynamics of the oil-water interface during biofilm formation and aging, we conducted active microrheology measurements with the ferromagnetic rods. At early age ($t_a < 2$ hrs), when the interfacial dynamics is dominated by the activity of the motile bacteria, the measurements involved the application of a field of strength $B$ rotating at constant angular frequency $\nu$ in the plane of the interface such that the rods rotated in response. Due to drag, the axis of the rod lagged the field by an angle $\psi$, providing a means of determining the drag viscosity. Specifically, in steady state the magnetic torque and drag torque on the rod are balanced,

$$\mu B\sin(\psi) = 2\pi\nu\gamma_R\eta_d, \tag{8}$$

where $\eta_d$ is the drag viscosity. Figure 6 displays results for $\sin(\psi)$ as a function of $\nu$ from measurements on a rod of length 31 $\mu$m in a rotating 10 G field. The line displays the result of a linear fit from which the drag viscosity of $\eta_d = 1.8 \pm 0.2$ mPa·s is obtained. Similar measurements on several other rods at active interfaces resulted in an average viscosity of $\eta_d = 2.2 \pm 0.4$ mPa·s. This is comparable to that obtained from similar measurements at the bare oil-water interface (3 ± 1 mPa·s), indicating that presence of the motile bacteria at early interface ages has little effect on the drag on the rod. Thus, the rod's rotational response to the torque from the external field contrasted with its spontaneous orientational fluctuations at early age, which as described above, were strongly enhanced over thermal diffusion due to the activity of the bacteria. Such contrasting behavior between passive and active measurements on a colloid implies a violation of the fluctuation-dissipation theorem in the active bath of swimming bacteria, an issue that has been considered previously[33,66,67].

The effective viscosity $\eta_{eff}$ found from the passive orientational fluctuations of the rod is greater than the drag viscosity on the actively rotated rod by roughly a factor of two. This difference could be the result of a reduced effective viscosity when performing a rheology measurement on an active bacterial suspension, as has been seen elsewhere[68–70]. However, such a reduction typically depends on shear rate, and the linearity of the data in Fig. 6 is an indication of a lack of any shear-rate dependence over the range of measured frequencies. Specifically, previous studies have noted

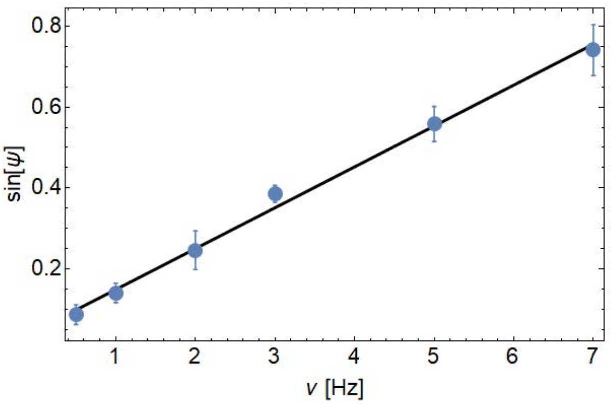

Fig. 6 Sine of the angle by which the orientation of a ferromagnetic rod of length 31 $\mu$m at the interface before biofilm formation lags a 10-G magnetic field that is rotating at frequency $\nu$. The solid line is the result of a linear fit whose slope is proportional to the drag torque on the rod.

the viscosity reduction is most pronounced at small applied shear rates, and the measured viscosity reverts to the solvent viscosity at high shear rate. The crossover between these behaviors can be parameterized in terms of a Peclet number that specifies the ratio of the applied shear rate to the swimming rate, as quantified by the bacteria diffusivity[70]. If one defines the Peclet number associated with the wire rotation as $\mathrm{Pe} = \nu/D_A$, then $\mathrm{Pe} \approx 120-1700$ over the range of measured $\nu$, suggesting the results in Fig. 6 are all in the limit of high Peclet number.

### 3.3 Active Microrheology of an Aging Biofilm

Once the biofilm formed, the viscoelastic nature of the film made measurements of the rods under constant rotation unfeasible. Instead, at later age the active measurements tracked the rotational response of a rod to the application of step-like changes in magnetic field between zero and a constant value $B$ in the plane of the interface at an angle $\phi_0$ to the rod's magnetic moment. An example of the resulting time-dependent angle of rotation $\theta$ away from its initial orientation is shown in Fig. 7 for a rod of length 34 $\mu$m in a film at age $t_a = 22$ hours. (The video of the interface from which the data was obtained is included in the SI.) At $t = 0$, a 57 G magnetic field was applied at $\phi_0 = 110^\circ$, causing the wire to rotate until the angle reached a plateau at $\theta \approx 46^\circ$ (*i.e.*, an angle of $\phi_0 - \theta \approx 64^\circ$ with respect to the field), at which point the magnetic torque on the rod was balanced by an elastic restoring torque from the film. The field was then set back to zero at $t = 22$ s, allowing the orientation of the rod to relax under the viscoelastic stresses of the film. Notably, the rod rotated back essentially fully to its initial equilibrium orientation, $\theta = 0$, indicating no unrecoverable strain and hence a rheological response of the biofilm that is characteristic of a viscoelastic solid. (Because of slight global rotation of the biofilm during these measurements, $\phi_0$, the angle between the field and the equilibrium orientation of the rod, typically changed by 2-3° over the course of the measurement, and the data are corrected for this variation.) We observed such viscoelastic-solid response in all measurements on fully formed biofilms, where we varied the strength of the applied field over the range 5-150 G and applied the magnetic torque for durations up to 2 minutes. Solid-like behavior on this timescale is consistent with previous studies of the mechanical properties of biofilms on solid substrates, in which an elastic relaxation time of approximately 20 minutes was observed for a range of systems[71].

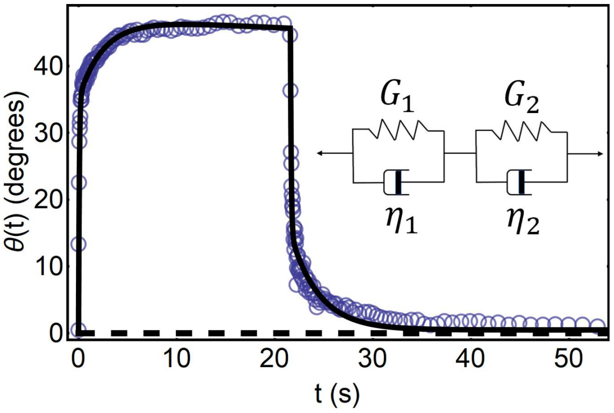

Fig. 7 The angle of rotation of a ferromagnetic rod within a biofilm at interface age 22 hours in response to a magnetic field and the viscoelastic torques from the film. At $t = 0$ a magnetic field of strength 57 G is applied at 110° to the rod's magnetic moment. The field is held constant until $t = 22$ s, when it is removed. The solid curve displays the result of a best fit to the data using a double Kelvin-Voigt model, shown schematically in the inset. The horizontal dashed line corresponds to the location of the rod's equilibrium orientation.

As Fig. 7 illustrates, the rotational response of the rod to the changes in magnetic field is characterized by an initial fast rotation followed by a slower terminal relaxation to the final angle. Viscoelastic behavior with multiple characteristic timescales has been observed previously in rheological measurements on biofilms grown on solid surfaces and reflects the multi-component, hierarchical microstructure of these biofilms. In those cases, the fastest timescale has been interpreted as being related to the flow of water and soluble polysaccharides within the biofilm, while the slower timescales were associated with the mechanical response of the EPS matrix and bacteria rearrangement within the biofilm.[72–74]. Fluid flow within the biofilm should result in a viscoelastic-fluid response, which is absent in our case, indicating such flow contributes negligibly to the measured rheology. Hence, we hypothesize the viscoelastic-solid behavior with two timescales results from the response of the crosslinked EPS matrix and the densely packed bacteria to the applied stress.

We find a viscoelastic model consisting of two Kelvin-Voigt spring-dashpot segments in series, depicted schematically in the inset of Fig. 7, describes the multi-component response in our results accurately. The model is described by the constitutive equations,

$$G_1\theta_1 + \eta_1\dot{\theta}_1 = -\frac{\mu B}{\gamma_{2D}} sin(\phi_0 - \theta), \tag{9}$$

$$G_2\theta_2 + \eta_2\dot{\theta}_2 = -\frac{\mu B}{\gamma_{2D}} sin(\phi_0 - \theta), \tag{10}$$

$$\theta = \theta_1 + \theta_2, \tag{11}$$

where $G_1$ and $G_2$ are the (two-dimensional) elasticities, and $\eta_1$ and $\eta_2$ are the (two-dimensional) viscosities associated with the springs and dashpots, respectively, $\theta_1$ and $\theta_2$ are the rotational strains of each Kelvin-Voigt segment, and $\gamma_{2D} = 1.48L^2$ is the geometrical coefficient for rotational drag on a rod in two dimensions[75]. We conducted least-squares fits to $\theta(t)$ using the model in which the data during both the rotational response to the field ($t < 22$ s) and subsequent zero-field rotational relaxation ($t > 22$ s) were fit simultaneously with four parameters: $\eta_1$, $\eta_2$, $G_1$, and $G_2$. As mentioned above, global rotation of the biofilm caused $\phi_0$ to change slightly ($\lesssim 5°$) during the experiment. Due to uncertainties associated with correcting for this bulk rotation, the best fit was given freedom to shift the relaxation segment of the fit along the y-axis by an amount up to an estimated maximum uncertainty of 0.5°. Figure 7 displays the result of the fit, which describes the data well and which results in the parameter values $\eta_1 = 33.7$ Pa·s·$\mu$m, $\eta_2 = 0.4$ Pa·s·$\mu$m, $G_1 = 11.6$ Pa·$\mu$m, and $G_2 = 5.3$ Pa·$\mu$m.

Such active microrheology experiments were performed on several biofilms, and measurements were conducted as the biofilms aged, providing temporal information of the films' viscoelastic properties. Measurements were initiated once the biofilm had formed sufficiently, as determined by the inability of the rod to align fully with the magnetic field ($t_a \approx 4$ hrs). Similarly good agreement with the double Kelvin-Voigt model to that in Fig. 7 was found for all the measurements. Figure 8 shows the parameters obtain from measurements on five biofilms. Surprisingly, within any trial the films showed no significant changes in viscoelastic parameters as a function of age, except perhaps for a slight increase in the elastic constants with age until $t_a \approx 10$ hours. Comparisons between trials further suggests the film viscosity was lower at larger ages. However, the viscoelastic parameters showed large variation between biofilms, which potentially reflected mesoscale heterogeneity in the film properties, making any comparisons between trials tentative. Overall, across the trials, the parameters had average values and standard deviations of $\eta_1 = 49 \pm 38$ Pa·s·$\mu$m, $\eta_2 = 0.80 \pm 0.76$ Pa·s·$\mu$m, $G_1 = 9.8 \pm 6.8$ Pa·$\mu$m, and $G_2 = 4.8 \pm 4.0$ Pa·$\mu$m. As the example in Fig. 7 illustrates, the elastic constants of the two Kelvin-Voigt were typically of similar magnitude, but on average $\eta_1 \approx 50\eta_2$. Measurements were conducted at field strengths from 5 to 150 Gauss, which resulted in rod rotations from equilibrium of 11° to 86°. We found no systematic variation in the fit parameters with field strength, indicating no measurable nonlinear component to the biofilm response[76], justifying the use of a linear model (Eqs. (9)-(11)) to describe the response of the film even in cases in which the rotated rod imposed large local strains. Further, we can estimate the Boussinesq number Bq for the rod motion in the viscoelastic film, which has a real part Bq $= \bar{\eta}/R\eta_b$[77], where $R$ is the rod radius, $\eta_b$ is the subphase viscosity, and $\bar{\eta}$ is an average of the interfacial viscosities, $\bar{\eta} = (\eta_1 + \eta_2/2)$. In all measurements except one, Bq $> 10^3$, justifying our neglect of subphase drag on the rod in the analysis.

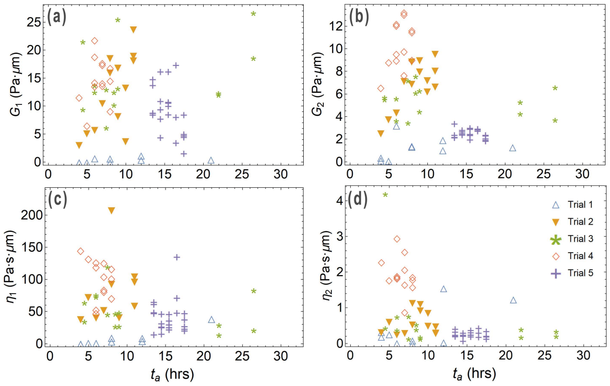

Fig. 8 Viscoelastic parameters (a) $G_1$, (b) $G_2$, (c) $\eta_1$, and (d) $\eta_2$ determined from fits using the double Kelvin-Voigt model to data like that in Fig. 7 obtained in five trials as a function of interface age.

Notably, the viscoelastic behavior of the biofilms measured in these active microrheology experiments is strikingly unlike the film rheology that one would infer from the MSDs of the 1-$\mu$m and 4-$\mu$m-diameter spherical colloids at late age shown in Fig. 2. One clear qualitative difference is the lack of a plateau in the MSDs that one would expect for a passive tracer in a viscoelastic solid. To make this comparison more concrete, we note that for a 2D medium in thermodynamic equilibrium, the MSDs are related to the creep compliance $J(t)$ through a generalized Stokes-Einstein relation[28],

$$\langle \Delta r^2(t) \rangle = \frac{2k_BT}{3\pi} J(t) \tag{12}$$

For the double Kelvin-Voigt system the creep compliance is

$$J(t) = \frac{1}{G_{eff}} - \frac{e^{-(G_1/\eta_1)t}}{G_1} + \frac{e^{-(G_2/\eta_2)t}}{G_2} \tag{13}$$

with $G_{eff} = G_1G_2/(G_1 + G_2)$. According to the active microrheological results, therefore, the MSDs of the spheres should show two time constants, $\eta_1/G_1$ and $\eta_2/G_2$, and should reach a plateau of $2k_BT/3\pi G_{eff}$ at large lag times. The time constants obtained from the measured viscoelastic parameters were on the order of fraction of a second for the fast time constant and tens of seconds for the slow time constant. As one can see from Fig. 2, the MSDs do not display any obvious structure on these timescales. Additionally, based on a typical value of $G_{eff}$ of 3 Pa·$\mu$m, the expected plateaus in the MSD should be at about $3 \times 10^{-4}$ $\mu$m$^2$, well below the actual MSDs of the 1-$\mu$m and 4-$\mu$m spheres shown in Fig. 2 and in fact below the resolution of the particle-tracking measurements. (Since the measured MSD of the 15-$\mu$m spheres in the biofilm is close to the estimated resolution, we cannot draw any quantitative conclusion about their apparent motion in comparison with the film rheology.)

A number of previous studies have noted large discrepancies between the rheology inferred from passive particle-tracking measurements of colloids at viscoelastic interfaces and the results of macroscopic interfacial rheology and have speculated about their origins[18,19,78]. While we are confident that the measurements avoided the systematic errors noted in these studies that could give rise to such discrepancies, the failure of Eqs. (12) and (13) to the describe the MSDs quantitatively is perhaps not surprising due to the possible effects of activity from persistent bacteria motility in the biofilm. However, such a strong and qualitative discrepancy implies a breakdown that goes beyond, for example, a simple "effective temperature" picture like that invoked above to describe the passive rod motion prior to biofilm formation. In our microscopy measurements after biofilm formation, fluctuations in the videos of the interface indicated the bacteria indeed retained some motility. Therefore, to understand the extent to which the bacteria remained motile, we performed differential dynamic microscopy (DDM) measurements, as described in the next section.

### 3.4 Differential Dynamic Microscopy of an Aging Biofilm

As mentioned above, one possible source of the discrepancy between the mobility of the spherical colloids in the biofilm and the microrheology of the film is the active nature of the film due to motion of the bacteria. Generally, bacteria can be motile or non-motile within biofilms. For example, an experiment performed with *Pseudomonas Aeruginosa* PA01 biofilms on solid substrates found a subpopulation of motile cells that moved on average 1.5 $\mu$m/hr with 90% of these cells moving less than about 6 $\mu$m/hr[79]. In other experiments, it has been shown that bacteria in the bulk fluid can penetrate and move within the biofilm[80]. While the microscopy videos of the biofilm at the oil-water interface at late ages showed clear evidence of persistent motion among bacteria, measuring their motility by tracking individual cells was unfeasible due to the high density and small size of the bacteria. Therefore, we employed differential dynamic microscopy (DDM) to circumvent these limitations. As described in Sec. 2.7, DDM involves measuring an ensemble quantity, the image structure function $D(q,t)$, which is related to the intermediate scattering function $g(q,t)$ via,

$$D(q,t) = A(q)(1-g(q,t)) + B(q) \tag{14}$$

where $A(q)$ depends on the spatial intensity correlations in the images, and $B(q)$ is due to digital noise. The intermediate scattering function, which has the limits $g(q,0) = 1$ and $g(q,t \to \infty) = 0$ for an ergodic system, is the spatial Fourier transform of the density autocorrelation function. A strength of DDM is its access to dynamics at larger wave vectors than can be reached with other techniques that measure $g(q,t)$, such as dynamic light scattering[48]. As a microscopy-based technique, DDM is also naturally suited to characterizing dynamics in quasi-two-dimensional systems when, like in our case, direct tracking is not feasible. DDM has been performed previously on suspensions of motile bacteria, as well as other soft and living matter, and has been shown to be a useful tool, for example, for extracting a diffusion constant for bacteria suspensions[47,48,81,82].

Figures 9(a) and (b) display~~s~~ $1-g(q,t)$ over the range of $0.1 < q < 5.7$ $\mu$m$^{-1}$ from DDM measurements at $t_a = 1$ hr, prior to biofilm formation, and at $t_a = 6$ hrs, after film formation. Figure S4 in the SI shows $D(q,t)$ for each data set from which $1-g(q,t)$ is obtained. (The videos from which the data are obtained are also included in the SI.) Also shown in Fig. 9(a) are the results of best fits to the pre-biofilm data using a diffusive, exponential form, $g(q,t) = e^{-t/\tau_D}$. Specifically, a fit to $D(q,t)$ was made at each wave vector with $\tau_D(q)$, $A(q)$, and $B(q)$ as parameters, and the results for $A(q)$ and $B(q)$ were used to extract the values of $1-g(q,t)$ and the fit results shown. The results for $A(q)$ and $B(q)$ along with additional details regarding the fitting procedure are provided in the SI. Figure 10 displays $\tau_D$ as a function of $q$ on a log-log plot. The line in the figure shows the result of a fit with the relation for diffusion, $\tau_D = 1/Dq^2$, where $D$ is the diffusion coefficient. The diffusive form approximates the data well, except perhaps at the lowest $q$. We note, however, $1-g(q,t)$ fails to reach its terminal plateau within the measured range of lag times at these lowest $q$, introducing greater uncertainty to the fitting at these wave vectors. Thus, the bacteria undergo diffusive dynamics at the interface at early ages. The diffusion constant obtained from the fit is $D = 0.86 \pm 0.01$ $\mu$m$^2$/s. For comparison, a 4-$\mu$m-diameter sphere undergoing thermal diffusion in water at room temperature has a diffusion coefficient $D \approx 0.1$ $\mu$m$^2$/s.

Another feature of the $\tau_D$ in Fig. 10 is the apparent small oscillations about the $q^{-2}$ dependence with a peak near $q_p = 0.6$ $\mu$m$^{-1}$. Notably, $A(q)$ and the Fourier transform of the images, shown in Fig. S6 in the SI, also show a peak at the same position, which could result from spatial correlations among the densely packed bacteria, equivalent to the structure factor peak of liquids. In this case, the peak in $\tau_D$ would indicate anomalously slow decay of density fluctuations at this wave vector, a phenomenon that is seen in inelastic neutron scattering of liquids and is known as de Gennes narrowing[83]. The effect is related to the collective nature of diffusion in dense fluids and specifically to the persistence of local packing arrangements among the diffusing particles.

At first glance, the observation that the diffusive behavior of the bacteria extends to the largest wave vectors is a bit surprising, since at the shortest length scales the swimming motion of the bacteria should lead to ballistic behavior wherein the correlation time of $g(q,t)$ should scale inversely with $q$ rather than $q^2$. We can estimate an upper bound for the length scale $l_D$ at which the motion crosses over to diffusion from the value of the largest measurement wave vector, $l_D \lesssim q_{max}^{-1} = 5.7^{-1}$ $\mu$m $\approx 0.18$ $\mu$m. This small upper bound indicates the bacteria's mean free path $l^*$ is only a fraction of the bacteria body length, which is consistent with the nearly close-packed density of bacteria at the interface. We can also estimate the mean free path through its relation with the diffusion coefficient, $D \approx v_s l^*/2$, where $v_s$ is the bacteria swimming speed. A previous study of *Pseudomonas Aeruginosa* PA14 at an oil-water interface measured a swimming speed of $v_s \approx 16$ $\mu$m/s[25], which corresponds to a mean free path of $l^* \approx 0.1$ $\mu$m, again only a fraction of the bacteria body length.

Once the viscoelastic biofilm forms, $g(q,t)$ no longer reaches zero over the range of measured lag times at any wave vector, signalling constrained motility of the bacteria. This loss of ergodicity creates a problem in the analysis because, if $D(q,t)$ does not reach a plateau that can be confidently associated with the terminal decay of $g(q,t)$, the factors $A(q)$ and $B(q)$ cannot be unambiguously determined. To circumvent this difficulty, we conducted DDM analysis of the microscopy images in which we shifted the images relative to each other at regular time intervals, which created an artificial de-correlation between images that forced $g(q,t)$ to zero at large lag times and enabled us to extract values for $A(q)$ and $B(q)$. Details regarding this analysis procedure are provided in the SI. An example of results from this analysis is displayed in

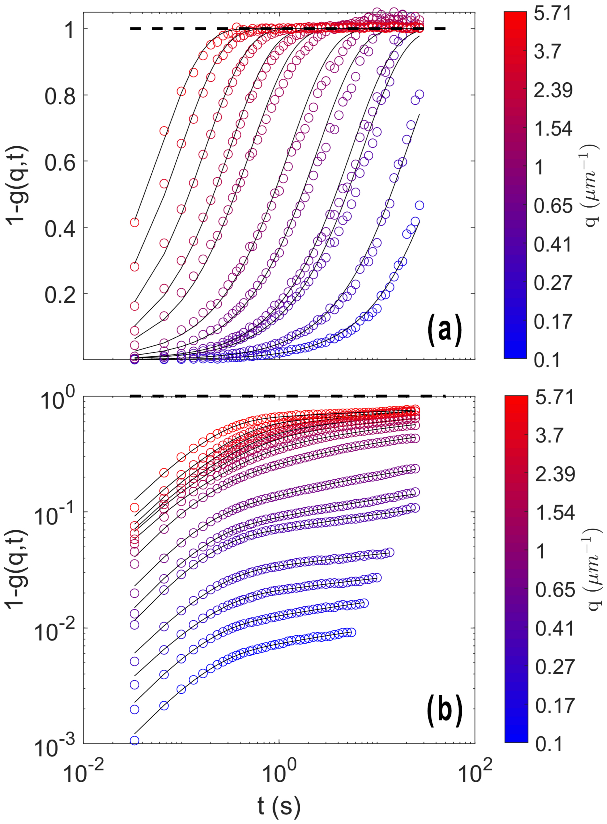

Fig. 9 One minus the intermediate scattering function obtained in DDM measurements of an interface at ages of (a) 1 hr and (b) 7 hrs. The data are color-coded by the values of the wave vector $q$, as indicated in the legends. The solid lines show the results of fits to the data, as described in the text.

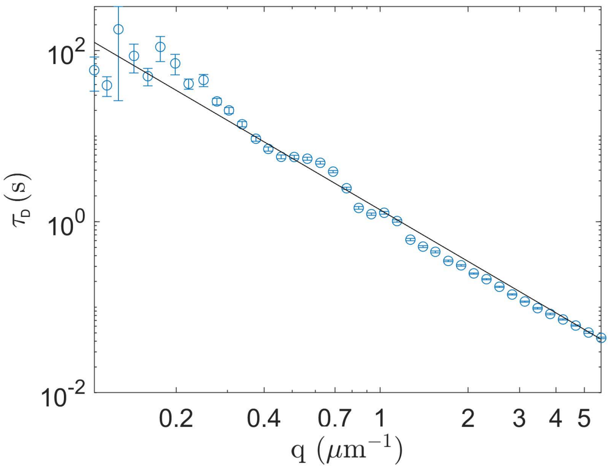

Fig. 10 Correlation time obtained from fits to $D(q,t)$ for the interface at age $t_a = 1$ hr as a function of wave vector. The solid line shows the result of a fit using the form $\tau = 1/Dq^2$ characteristic of diffusive dynamics.

Fig. 9(b), which shows $1-g(q,t)$ at $t_a = 7$ hrs. The intermediate scattering functions show an initial decay at short lag times to a quasi-plateau at a value that depends on wave vector, followed by a much slower decay at larger lag times. DDM measurements on interfaces at other late ages ($t_a > 5$ hrs) gave similar results. Such partial decays to a quasi-plateau are familiar from glassy fluids where the decay is associated with localized, caged motion of the particles. With formation of the biofilm, the bacteria motility apparently becomes similarly constrained.

To analyze the bacteria dynamics in the biofilm quantitatively, we fit the intermediate scattering functions using a sum of an exponential and a power law to capture the initial decay at small lag times and the slow relaxation at large lag times, respectively,

$$g(q,t) = \lambda e^{-t/\tau_1} + (1-\lambda)(\frac{t+\tau_2}{\tau_2})^{-\alpha}. \tag{15}$$

Results of such fits are are shown by the lines in Fig. 9(b). The fit parameters $\tau_1$ and $\tau_2$ along with further details regarding the fitting procedure are described in the SI. Here, we focus on interpreting the other fit parameters, $\lambda$ and $\alpha$, which characterize the magnitude of the initial decay and the late-time power-law behavior, respectively. As mentioned above, the initial decay in $g(q,t)$ is indicative of constrained, localized motion of the bacteria on short timescales. For localized particles whose dynamics are uncorrelated and obey Gaussian statistics, $g(q,t)$ decays to $e^{-r_{loc}^2 q^2/4}$, where $r_{loc}$ is an average localization length[84], or equivalently from Eq. (15), $1-\lambda = e^{-r_{loc}^2 q^2/4}$. Figure 11(a) displays $\ln(1-\lambda)$ plotted against $q^2$. Over much of the measured range, the expected linear form is observed. The line in Fig. 11(a) displays the result of a linear fit to the data for $q^2 > 10\ \mu\text{m}^{-2}$, from which we find $r_{loc} = 0.15\ \mu$m. In principle, $(1-\lambda)$ should go to one as $q \to 0$. The non-zero $y$-intercept of the fit result in Fig. 11(a) could be due to either a contribution to the DDM signal from bacteria that are not localized, for example bacteria that are moving in the aqueous phase above the biofilm, or from small systematic errors in $A(q)$ at low $q$, where the factor has the greatest uncertainty.

The dynamics of the bacteria in the biofilm are not bounded by $r_{loc}$ on all time scales, however, as the power-law decay in $g(q,t)$ at large lag times indicates slow, de-localized motion. Figure 11(b) displays the power-law exponents $\alpha$ obtained from the fits shown in Fig. 9(b) as a function of wave vector. The exponents have dependence of wave vector whose origin is not immediately clear, but they maintain small values, $\alpha < 0.2$, over the full range. This weak power-law behavior is similar to the weak power-law growth of the MSDs of the 4-$\mu$m and 15-$\mu$m colloids at late interface age seen in Fig. 2, suggesting the long-time dynamics of the bacteria in the biofilm qualitatively resembles that of the passive tracers.

## 4 Discussion and Conclusion

This study has combined three techniques – passive particle tracking, active microrheology, and DDM – in a multi-pronged approach to understand the evolution of an oil-water interface during biofilm formation. In this section, we discuss how one might synthesize the findings from the different measurements and their

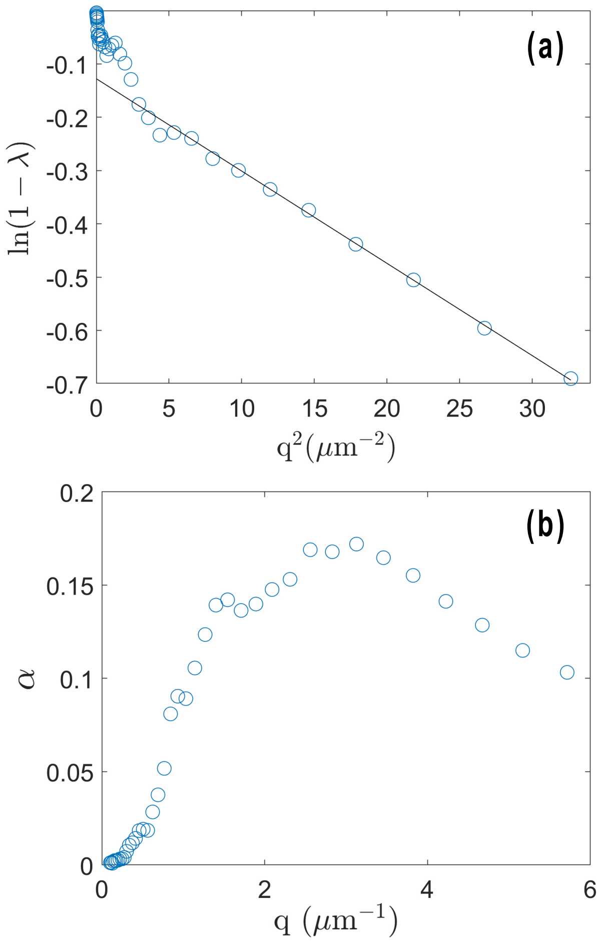

Fig. 11 (a) Logarithm of one minus $\lambda$, the value of the quasi-plateau in $g(q,t)$, as a function of wave-vector squared, and (b) power-law exponent $\alpha$ characterizing the large lag-time decay of $g(q,t)$ from the DDM measurements at interface age $t_a = 7$ hr. The solid line in (a) shows the result of a linear fit.

implications for the evolution of the interface properties. The three sets of measurements all show behavior consistent with a transition in interfacial properties at an age between three and five hours. At early age the properties are dominated by a large interfacial concentration of highly motile adsorbed bacteria, while at later age they are strongly affected by the restructuring of the interface associated with biofilm formation. The active microrheology shows conclusively that, once fully formed ($t_a \gtrsim 4$ hrs), the biofilm acts as a viscoelastic solid on length scales of tens of micrometers. Perhaps the most intriguing question to arise from this observation is how to reconcile this finding with the passive particle tracking measurements. The persistent mobility of the spheres in the well-formed biofilm is, in itself, not surprising in light of the DDM measurements that showed the bacteria continued moving in the biofilm, thereby providing a continued source of activity to the system. Indeed, with the microrheology of the environment known, one could in principle extract from the passive particle MSDs the force spectrum associated with the activity[85,86]. However, applying such analysis to the MSDs of the spherical colloids is problematic due to the widely differing mobilities of the spheres of different diameter. In short, within such analysis either the biofilm's rheological response or the active force spectrum must have a length-scale dependence to reconcile the orders-of-magnitude difference between the MSDs of the 1-$\mu$m-diameter and 15-$\mu$m-diameter spheres.

One possible source of concern is that the large MSDs of the smaller spheres could be an artifact of the biofilm acquiring anomalous local properties in vicinity to these colloids, for example due to depletion of extracellular polymeric substances secreted by the bacteria. Such local effects are known to be an issue in single-particle passive microrheology[28]. However, the three sets of spheres of different diameter employed in the measurements all had the same non-functionalized surfaces, which were designed by the manufacturer to be suitable for coating with biopolymers via adsorption[87]. Indeed, this proclivity for adsorption could explain the anecdotal observations mentioned above that the spheres tended act as nucleation sites for biofilm growth in the early stages of formation. It also suggests that the spheres would become well coupled mechanically to the biofilm as it formed and hence not reside in regions of locally anomalous rheology. Regardless, since all the spheres had the same surface chemistry, any local anomalies in biofilm processes due to surface-specific interactions would presumably affect all three sets of spheres and hence could not explain the divergent mobilities among the three sizes. However, we cannot rule out that the 1-$\mu$m and 4-$\mu$m spheres by virtue of their size might reside in anomalously soft regions of the biofilm that are inaccessible to the 15-$\mu$m spheres. Further studies that employ spheres with different surface chemistry would help clarify the potential effect of sphere-film or sphere-bacteria interactions on the sphere mobility.

A possible clue to the origin of the discrepancies between the sphere mobility and the active microrheology of the biofilms comes from considering the sizes and geometries of the colloids. As mentioned above, the divergence in mobilities of the different-sized spheres suggests that the mechanical properties of the biofilm could be length-scale dependent. The rods employed in the active microrheology were 30-75 $\mu$m in length and rotated through large angles, thereby probing the rheology on length scales comparable to their length. Notably, in the particle-tracking measurements the 15-$\mu$m spheres, whose size most closely matched that of the rods, became essentially immobile once the biofilms formed, qualitatively consistent with the viscoelastic-solid behavior measured in the active rheology. The dramatically higher mobility of the 4-$\mu$m and especially the 1-$\mu$m spheres thus suggests that the biofilms might have hierarchical mechanical properties such that they are significantly more compliant and fluid-like at the smaller scales of these particles. The mesh size of the extracellular polymer matrix of the biofilms is likely much smaller than the colloids[7]; therefore, we do not anticipate the mesh size has any direct influence. Notably, however, the bacteria, which are 1-5 $\mu$m in length, have a size that is similar to that of the smaller, more mobile spheres. This similarity suggests an intriguing speculation that the biofilms potentially form with a hierarchical mechanical structure that has a compliant, glassy fluid rheology on the scale of the bacteria to facilitate their motility[80] in the films but more rigid, solid-like rheology on larger length scales to maintain mechanical integrity. Experiments combining passive particle tracking and active microrheology, such as for example by use of an optical trap, on the same small spheres would help better determine the mechanical environment of the spheres and its relation to their positional fluctuations.

Another possible source of the discrepancies between the mobility of the smaller spheres and the active microrheology could be the activity of the bacteria within the biofilm. Just as the particle tracking measurements on the spheres and rods at the interface prior to biofilm formation revealed diffusive and even super-diffusive motion dominated by the interactions with the swimming bacteria, so potentially could residual bacteria motility in the biofilms induce probe motion. The DDM measurements convey a picture of the bacteria dynamics at the interface that potentially provides insight into the passive colloidal mobility. As described above, the bacteria motility evolves from diffusive motion characteristic of a concentrated but disordered assembly of unconstrained swimming bacteria at early age to constrained but ultimately unbounded motion within the viscoelastic biofilm at later age. Details aside, a key observation from the DDM measurements is the continued motility of the bacteria in the biofilm at late age, which presumably affects the motion of the spheres in the passive particle tracking measurements and explains, at least in part, the decoupling of the motion of the 1-$\mu$m and 4-$\mu$m spheres from the film rheology. One avenue for further study to understand better the influence of bacteria activity on sphere motion would be to examine any spatial heterogeneities in the bacteria motion. As seen in Fig. 4, the sphere mobility in the biofilm is heterogeneous. Identifying spacial correlations in this heterogeneity with that in the bacteria activity would help characterize dynamic coupling between spheres and bacteria. Since the DDM technique measures the bacteria motion in Fourier space, it does not provide spatially resolved information needed to distinguish spatial correlations in particle dynamics and bacterial motility, and an alternative approach would need to be found to interrogate spatial variations in bacteria activity.

The fact that the 1-$\mu$m and 4-$\mu$m spheres, which are much more strongly affected than the 15-$\mu$m spherse, are similar in size to the bacteria themselves is perhaps not a coincidence. Indeed, when a colloidal probe is comparable in size to the constituent particles of the medium, the validity of typical macroscopically derived formulas can no longer be assumed to hold[88]. An interesting question is how the large-time, slow dynamics of the bacteria captured in the DDM might reflect the same "passive" motion experienced by the smaller spheres. That is, one has a picture in which the bacteria becomes caught in the viscoelastic solid biofilm but nevertheless continue to exert forces on their environment. This collective activity provides a nonthermal energy source to the system that ultimately leads to delocalization not only of the colloids but also of the bacteria themselves.

## Conflicts of interest

There are no conflicts to declare.

## Acknowledgements

We thank Liana Vaccari, Tagbo Niepa, and James Harden for helpful discussions. Funding was provided by the NSF (CBET-1804721 and DMR-1610875).

## Notes and references

1 R. M. Donlan, Emerging Infectious Disease journal, 2002, **8**, 881.

2 M. Simões, L. C. Simões and M. J. Vieira, LWT - Food Science and Technology, 2010, **43**, 573 – 583.

3 M. Omarova, L. T. Swientoniewski, I. K. Mkam Tsengam, D. A. Blake, V. John, A. McCormick, G. D. Bothun, S. R. Raghavan and A. Bose, ACS Sustainable Chem. Eng., 2019, **7**, 14490–14499.

4 B. Erable, N. M. Duţeanu, M. Ghangrekar, C. Dumas and K. Scott, Biofouling, 2010, **26**, 57–71.

5 B. E. Logan, Nature Reviews Microbiology, 2009, **7**, 375–381.

6 L. Qi and G. F. Christopher, Langmuir, 2019, **35**, 5294–5304.

7 J. N. Wilking, T. E. Angelini, A. Seminara, M. P. Brenner and D. A. Weitz, MRS Bulletin, 2011, **36**, 385–391.

8 O. Lieleg, M. Caldara, R. Baumgärtel and K. Ribbeck, Soft Matter, 2011, **7**, 3307–3314.

9 M. Böl, A. E. Ehret, A. B. Albero, J. Hellriegel and R. Krull, Critical Reviews in Biotechnology, 2013, **33**, 145–171.

10 P. A. Araújo, J. Malheiro, I. Machado, F. Mergulhão, L. Melo and M. Simões, Journal of Environmental Engineering, 2016, **142**, 04016031.

11 P. Stoodley, R. Cargo, C. J. Rupp, S. Wilson and I. Klapper, Journal of Industrial Microbiology and Biotechnology, 2002, **29**, 361–367.

12 P. A. Rühs, L. Böni, G. G. Fuller, R. F. Inglis and P. Fischer, PLOS ONE, 2013, **8**, e78524.

13 P. Rühs, L. Böcker, R. Inglis and P. Fischer, Colloids and Surfaces B: Biointerfaces, 2014, **117**, 174 – 184.

14 T. H. Niepa, L. Vaccari, R. L. Leheny, M. Goulian, D. Lee and K. J. Stebe, Scientific Reports, 2017, **7**, 17864.

15 E. C. Hollenbeck, C. Douarche, J.-M. Allain, P. Roger, C. Regeard, L. Cegelski, G. G. Fuller and E. Raspaud, The Journal of Physical Chemistry B, 2016, **120**, 6080–6088.
16 Y.-J. Lin, S. Barman, P. He, Z. Zhang, G. F. Christopher and S. L. Biswal, Journal of Rheology, 2018, **62**, 1–10.
17 E. Hollenbeck, J. Fong, J. Lim, F. Yildiz, G. Fuller and L. Cegelski, Biophysical Journal, 2014, **107**, 2245 – 2252.
18 J. R. Samaniuk and J. Vermant, Soft Matter, 2014, **10**, 7023–7033.
19 E. Guzmán, J. Tajuelo, J. M. Pastor, M. Ángel Rubio, F. Ortega and R. G. Rubio, Current Opinion in Colloid & Interface Science, 2018, **37**, 33 – 48.
20 A. Koza, P. D. Hallett, C. D. Moon and A. J. Spiers, Microbiology, 2009, **155**, 1397–1406.
21 C. Wu, J. Lim, G. Fuller and L. Cegelski, Biophysical Journal, 2012, **103**, 464 – 471.
22 C. Wu, J. Y. Lim, G. G. Fuller and L. Cegelski, Langmuir, 2013, **29**, 920–926.
23 M. Trejo, C. Douarche, V. Bailleux, C. Poulard, S. Mariot, C. Regeard and E. Raspaud, Proceedings of the National Academy of Sciences, 2013, **110**, 2011–2016.
24 L. Vaccari, D. B. Allan, N. Sharifi-Mood, A. R. Singh, R. L. Leheny and K. J. Stebe, Soft Matter, 2015, **11**, 6062–6074.
25 L. Vaccari, M. Molaei, T. H. Niepa, D. Lee, R. L. Leheny and K. J. Stebe, Advances in Colloid and Interface Science, 2017, **247**, 561 – 572.
26 G. Subbiahdoss and E. Reimhult, Colloids and Surfaces B: Biointerfaces, 2020, **194**, 111163.
27 J. C. Conrad, Journal of Industrial Microbiology & Biotechnology, 2020, **47**, 725–738.
28 T. M. Squires and T. G. Mason, Annual Review of Fluid Mechanics, 2010, **42**, 413–438.
29 A. J. Levine and T. C. Lubensky, Phys. Rev. Lett., 2000, **85**, 1774–1777.
30 X.-L. Wu and A. Libchaber, Phys. Rev. Lett., 2000, **84**, 3017–3020.
31 G. Miño, T. E. Mallouk, T. Darnige, M. Hoyos, J. Dauchet, J. Dunstan, R. Soto, Y. Wang, A. Rousselet and E. Clement, Phys. Rev. Lett., 2011, **106**, 048102.
32 R. Jeanneret, D. O. Pushkin, V. Kantsler and M. Polin, Nature Communications, 2016, **7**, 12518.
33 C. Maggi, M. Paoluzzi, L. Angelani and R. Di Leonardo, Scientific Reports, 2017, **7**, 17588.
34 A. E. Patteson, A. Gopinath, P. K. Purohit and P. E. Arratia, Soft Matter, 2016, **12**, 2365–2372.
35 Y. Peng, L. Lai, Y.-S. Tai, K. Zhang, X. Xu and X. Cheng, Phys. Rev. Lett., 2016, **116**, 068303.
36 E. F. Semeraro, J. M. Devos and T. Narayanan, The Journal of Chemical Physics, 2018, **148**, 204905.
37 L. Ortlieb, S. Rafaï, P. Peyla, C. Wagner and T. John, Phys. Rev. Lett., 2019, **122**, 148101.
38 E. L. C. V. M. Plan, J. M. Yeomans and A. Doostmohammadi, Phys. Rev. Fluids, 2020, **5**, 023102.
39 M. Tanase, L. A. Bauer, A. Hultgren, D. M. Silevitch, L. Sun, D. H. Reich, P. C. Searson and G. J. Meyer, Nano Lett., 2001, **1**, 155–158.
40 N. P. Mortensen, J. D. Fowlkes, C. J. Sullivan, D. P. Allison, N. B. Larsen, S. Molin and M. J. Doktycz, Langmuir, 2009, **25**, 3728–3733.
41 C. M. Toutain, M. E. Zegans and G. A. O'Toole, Journal of Bacteriology, 2005, **187**, 771–777.
42 M. H. Lee, C. P. Lapointe, D. H. Reich, K. J. Stebe and R. L. Leheny, Langmuir, 2009, **25**, 7976–7982.
43 D. B. Allan, T. A. Caswell, N. Keim, F. Boulogne, R. W. Perry and L. Uieda, trackpy: Trackpy v0.3.3, 2014.
44 J. C. Crocker and D. G. Grier, Journal of Colloid and Interface Science, 1996, **179**, 298 – 310.
45 D. B. Allan, D. M. Firester, V. P. Allard, D. H. Reich, K. J. Stebe and R. L. Leheny, Soft Matter, 2014, **10**, 7051–7060.
46 F. Giavazzi, D. Brogioli, V. Trappe, T. Bellini and R. Cerbino, Phys. Rev. E, 2009, **80**, 031403.
47 R. Cerbino and P. Cicuta, The Journal of Chemical Physics, 2017, **147**, 110901.
48 L. G. Wilson, V. A. Martinez, J. Schwarz-Linek, J. Tailleur, G. Bryant, P. N. Pusey and W. C. K. Poon, Phys. Rev. Lett., 2011, **106**, 018101.
49 J.-L. Thiffeault, Phys. Rev. E, 2015, **92**, 023023.
50 P. G. Saffman and M. Delbrück, Proceedings of the National Academy of Sciences, 1975, **72**, 3111–3113.
51 T. M. Fischer, P. Dhar and P. Heinig, Journal of Fluid Mechanics, 2006, **558**, 451–475.
52 I. M. Sokolov, Soft Matter, 2012, **8**, 9043–9052.
53 J.-H. Jeon, N. Leijnse, L. B. Oddershede and R. Metzler, New Journal of Physics, 2013, **15**, 045011.
54 S. C. Weber, A. J. Spakowitz and J. A. Theriot, Phys. Rev. Lett., 2010, **104**, 238102.
55 L. Vaccari, M. Molaei, R. L. Leheny and K. J. Stebe, Soft Matter, 2018, **14**, 5643–5653.
56 C. Maggi, M. Paoluzzi, N. Pellicciotta, A. Lepore, L. Angelani and R. Di Leonardo, Phys. Rev. Lett., 2014, **113**, 238303.
57 M. M. Tirado, C. L. Martínez and J. G. de la Torre, The Journal of Chemical Physics, 1984, **81**, 2047–2052.
58 D. Loi, S. Mossa and L. F. Cugliandolo, Phys. Rev. E, 2008, **77**, 051111.
59 J. Palacci, C. Cottin-Bizonne, C. Ybert and L. Bocquet, Phys. Rev. Lett., 2010, **105**, 088304.
60 K. C. Leptos, J. S. Guasto, J. P. Gollub, A. I. Pesci and R. E. Goldstein, Phys. Rev. Lett., 2009, **103**, 198103.
61 S. C. Takatori, R. De Dier, J. Vermant and J. F. Brady, Nature Communications, 2016, **7**, 10694.
62 A. Argun, A.-R. Moradi, E. Pinçe, G. B. Bagci, A. Imparato and G. Volpe, Phys. Rev. E, 2016, **94**, 062150.
63 M. M. Tirado and J. G. de la Torre, The Journal of Chemical Physics, 1979, **71**, 2581–2587.
64 O. Yang, Y. Peng, Z. Liu, C. Tang, X. Xu and X. Cheng, Phys. Rev. E, 2016, **94**, 042601.
65 R.-k. Xu, H.-j. Jiang and Z.-h. Hou, Chinese Journal of

Chemical Physics, 2021, **34**, 157–164.

66 D. T. N. Chen, A. W. C. Lau, L. A. Hough, M. F. Islam, M. Goulian, T. C. Lubensky and A. G. Yodh, Phys. Rev. Lett., 2007, **99**, 148302.

67 E. W. Burkholder and J. F. Brady, The Journal of Chemical Physics, 2019, **150**, 184901.

68 A. Sokolov and I. S. Aranson, Phys. Rev. Lett., 2009, **103**, 148101.

69 H. M. López, J. Gachelin, C. Douarche, H. Auradou and E. Clément, Phys. Rev. Lett., 2015, **115**, 028301.

70 J. Y. Y. Chui, C. Douarche, H. Auradou and R. Juanes, Soft Matter, 2021, –.

71 T. Shaw, M. Winston, C. J. Rupp, I. Klapper and P. Stoodley, Phys. Rev. Lett., 2004, **93**, 098102.

72 B. W. Peterson, H. C. van der Mei, J. Sjollema, H. J. Busscher, P. K. Sharma, M. Chapman and S. J. Hultgren, mBio, 2013, **4**, e00497–13.

73 Y. He, B. W. Peterson, M. A. Jongsma, Y. Ren, P. K. Sharma, H. J. Busscher and H. C. van der Mei, PLOS ONE, 2013, **8**, e63750.

74 B. W. Peterson, Y. He, Y. Ren, A. Zerdoum, M. R. Libera, P. K. Sharma, A.-J. van Winkelhoff, D. Neut, P. Stoodley, H. C. van der Mei and H. J. Busscher, FEMS Microbiology Reviews, 2015, **39**, 234–245.

75 A. J. Levine, T. B. Liverpool and F. C. MacKintosh, Phys. Rev. Lett., 2004, **93**, 038102.

76 S. Jana, S. G. V. Charlton, L. E. Eland, J. G. Burgess, A. Wipat, T. P. Curtis and J. Chen, npj Biofilms and Microbiomes, 2020, **6**, 19.

77 S. Reynaert, C. F. Brooks, P. Moldenaers, J. Vermant and G. G. Fuller, Journal of Rheology, 2008, **52**, 261–285.

78 F. Ortega, H. Ritacco and R. G. Rubio, Current Opinion in Colloid & Interface Science, 2010, **15**, 237 – 245.

79 A. R. Rice, M. A. Hamilton and A. K. Camper, Microbial Ecology, 2003, **45**, 163–172.

80 A. Houry, M. Gohar, J. Deschamps, E. Tischenko, S. Aymerich, A. Gruss and R. Briandet, Proceedings of the National Academy of Sciences, 2012, **109**, 13088–13093.

81 A. Jepson, V. A. Martinez, J. Schwarz-Linek, A. Morozov and W. C. K. Poon, Phys. Rev. E, 2013, **88**, 041002.

82 J. H. Cho, R. Cerbino and I. Bischofberger, Phys. Rev. Lett., 2020, **124**, 088005.

83 J. Hansen and I. R. McDonald, Theory of simple liquids : with applications to soft matter, Academic Press, 2013.

84 B. J. Berne and R. Pecora, Dynamic Light Scattering with Applications to Chemistry, Biology, and Physics, Dover, Mineola, 2000.

85 A. W. C. Lau, B. D. Hoffman, A. Davies, J. C. Crocker and T. C. Lubensky, Phys. Rev. Lett., 2003, **91**, 198101.

86 M. Guo, A. Ehrlicher, M. Jensen, M. Renz, J. Moore, R. Goldman, J. Lippincott-Schwartz, F. Mackintosh and D. Weitz, Cell, 2014, **158**, 822 – 832.

87 Bangs Laboratories, Inc., Technote 204.

88 D. Coglitore, S. P. Edwardson, P. Macko, E. A. Patterson and M. Whelan, Royal Society Open Science, 2017, **4**, 170507.